Rare Metal Materials and Engineering
Volume 51, Issue 10, October 2022
Available online at www.rmme.ac.cn

Science Press

Cite this article as: Zhang Jianguo, Huang Daoyu, Hu Fengling, et al. Mechanical Properties of Ti6Al4V Alloy with Porous Structure Prepared by Selective Laser Melting[J]. Rare Metal Materials and Engineering, 2022, 51(10): 3619-3625.

ARTICLE

Mechanical Properties of Ti6Al4V Alloy with Porous Structure Prepared by Selective Laser Melting

Zhang Jianguo[1], Huang Daoyu[1], Hu Fengling[2], Chen Chen[1], Song Liang[3], Zhou Qiong[1], Zhang Ergeng[1]

[1] Shanghai Engineering Research Center of Physical Vapor Deposition (PVD) Superhard Coating and Equipment, School of Mechanical Engineering, Shanghai Institute of Technology, Shanghai 201418, China; [2] Department of Stomatology, Zhongshan Hospital, Fudan University, Shanghai 200032, China; [3] Department of Stomatology, Shanghai Fifth People's Hospital, Fudan University, Shanghai 200240, China

Abstract: The optimized manufacturing route of selective laser melting (SLM) for Ti6Al4V alloy was simulated by Simufact Additive software through orthogonal experiment. The results show that laser power 200 W, scanning speed 1200 mm/s, spot diameter 0.1 mm and powder thickness 0.03 mm are the optimal processing parameters. Samples with different pore structures were fabricated by SLM according to the optimized parameters, and scanning electron microscopy images show that the porous structures processed by this process have better fidelity. The compressive strength and elastic modulus of solid and different pore structures were compared and analyzed through compression experiments. It is concluded that the composite structure as the structural model of the implant can better meet the requirement for mechanical properties of the implant.

Key words: SLM; Ti6Al4V alloy; porous structure; mechanical properties

Since Branemark et al[1] first proposed the theory of osseointegration in the 1860s, and took the lead in using pure titanium to make dental implants. With more than 60 years of development, dental implant technology has been widely used in clinical practice, and to a large extent implant restoration has replaced a variety of conventional restoration methods, which has become an important means of restoring dentition defects and missing dentition[2,3]. However, the currently used implants are solid cylindrical or solid conical implants, which are quite different from the natural root morphology. This kind of morphology, fortunately, can be achieved by making the implants into porous materials [4].

In order to realize immediate planting of bionic implants similiar to the natural root morphology, Ding et al[5] applied pure titanium casting technology to develop pure titanium bionic implants, and successfully completed animal experiments and clinical studies with satisfactory results. In recent years, with the application of 3D printing technology[6,7], additive manufacturing technology provides a new research idea for manufacturing personalized dental implant. Moin et al[8] produced personalized titanium alloy bionic implants that are consistent with the original tooth roots through SLM, laying the foundation for the development of 3D printing technology in the field of dental implants. Mangano et al[9] used 3D laser printing technology to manufacture personalized titanium alloy root implants, which were immediately implanted into the patient's alveolar socket after tooth extraction, and achieved good clinical results.

Ti6Al4V (TC4) alloy has the advantages of low density, high specific strength and good biocompatibility[10]. It has better comprehensive mechanical properties than traditional implant metal materials[11], and the usage rate of bone and dental implant materials is higher.

The elastic modulus of titanium alloy far exceeds that of the human body's natural bone, resulting in the phenomenon of "stress shielding", which ultimately leads to the failure of the implant[12,13].

At present, the commonly used Ti6Al4V implants in

Received date: November 12, 2021
Foundation item: Natural Science Foundation of Shanghai (19ZR1455100); Natural Science Research Project of Minhang District, Shanghai (2019MHZ039)
Corresponding author: Song Liang, Master, Deputy Chief Physician, Department of Stomatology, Shanghai Fifth People's Hospital, Fudan University, Shanghai 200240, P. R. China, E-mail: xuezhewenbo@163.com

clinical practice are basically compact structures, and their elastic modulus (105~120 GPa) is significantly higher than that of human natural bone (0.05~30 GPa). After long-term implantation, it will produce a "stress shielding" effect, which will not only cause the tissue around the implant to shrink and cause the implant to loosen, fall off and break, but also easily cause excessive micro-movement of the interface between the implant and the bone tissue, accumulation of plaque, and then cause peri-implant inflammation, and ultimately lead to implant failure[14-17].

In order to solve the "stress shielding" problem, we designed the implant to have a porous structure. At present, the most effective method is to design a porous unit structure in the metal implant[18]. The mechanical property of porous metal foams can be adjusted availably by controlling the porosity of the porous product[19,20]. By changing the design parameters of the porous unit structure, the most suitable elastic modulus match for the implant and the human bone can be achieved[21,22]. At the same time, the porous structure can also promote the transportation of nutrients and metabolic wastes, and provide the possibility for bone ingrowth[23-26].

Although the traditional porous metal preparation method[27] can also realize the manufacture of porous structure, it cannot produce a more complex pore structure, and there is a problem that it cannot be accurately manufactured[28]. SLM[29] can form high-density parts and can be used to study the mechanical properties of a variety of metal materials under different laser processing conditions[30].

Three-dimensional software was used to create three specimens with different spatial pore structures, and three sets of specimens with different spatial pore structures (regular hexahedral structure, G7 structure, and composite structure) were formed using SLM.

Simufact Additive software was used to find the best process route for SLM fabrication. The compressive elastic modulus and compressive strength of three different porous structures were investigated by mechanical tests. The fracture morphology after compression deformation was observed by scanning electron microscope (SEM). The mechanical properties of porous structures fabricated by SLM were analyzed and compared.

1 Experiment

The laser rapid prototyping equipment produced by the German EOS company was used, and its model was EOSINT M 280. The equipment was loaded with a Yb-fiber laser transmitter, the maximum molding size was 250 mm×250 mm×325 mm, argon can be used as a protective atmosphere, and the minimum oxygen concentration can be controlled within 0.1%. The density of parts can reach more than 98%[31,32].

The shape of Ti6Al4V (TC4) powder used in this study was spherical, and the particle size was 20~45 μm. The theoretical density was 4.43 g/cm^3, the loose density of the powder was 2.50 g/cm^3, and the tap density was 2.80 g/cm^3. The chemical composition is shown in Table 1, and the particle morphology is shown in Fig. 1. It shows that Ti6Al4V (TC4) powder has good sphericity.

The apparent morphology of the samples manufactured by SLM, and the compression morphology of the compression deformation after wire-cutting, were observed using the Nova Nano SEM 430 (FEI, USA) scanning electron microscope (SEM).

2 Results and Discussion

In this experiment, three specimens with different porous structures were designed; the outer pore size of the unit cell is 500 μm, the inner pore size is 400 μm, and the porosity is 40%~60%. In order to improve the printing efficiency and printing quality, we first simulated the best process route through the Simufact Additive software for the printing process of the porous structure.

The parameters of SLM printing and manufacturing include laser power, scanning speed, spot diameter, powder thickness, etc. We set the diameter of the spot to be 0.1 mm and the thickness of the powder to be 0.03 mm (Table 2). The parameters of laser power and scanning speed were set as the variable amount, the spot diameter and the powder thickness were set as fixed amounts, an orthogonal experiment was established, and the best process parameters were studied. The selection range of the parameters is shown in Table 3.

The spatial structure and solid structure of the unit cells of the samples with three different pore structures are shown in Fig.2.

We used Simufact Additive software to simulate the printing and manufacturing process, and the best processing parameters were determined through the range of stress and

Table 1 Chemical composition of Ti6Al4V powder

Al	V	Fe	C	N	H	O	Ti
6.4	4.0	0.17	0.016	0.018	0.002	0.12	Bal.

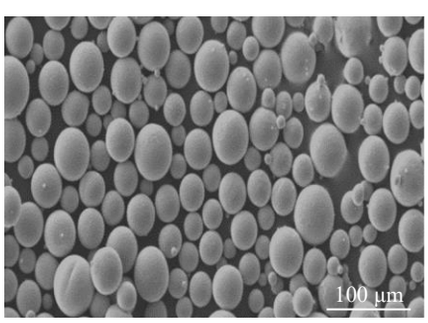

Fig.1 Particle morphology of TC4 powder

Table 2 Parameter values of SLM process

Parameter	Value
Layer thickness/mm	0.03
Hatch spacing/mm	0.10
Laser power/W	200, 300, 400
Scanning speed/mm·s^{-1}	1000, 1100, 1200

Table 3 Parameters of orthogonal array for L9 (3^3)

Experiment No.		Regular hexahedral structure	G7 structure	Composite structure
1	Laser/W	200	200	200
	Scanning speed/mm·s^{-1}	1000	1000	1000
2	Laser/W	200	200	200
	Scanning speed/mm·s^{-1}	1100	1100	1100
3	Laser/W	200	200	200
	Scanning speed/mm·s^{-1}	1200	1200	1200
4	Laser/W	300	300	300
	Scanning speed/mm·s^{-1}	1000	1000	1000
5	Laser/W	300	300	300
	Scanning speed/mm·s^{-1}	1100	1100	1100
6	Laser/W	300	300	300
	Scanning speed/mm·s^{-1}	1200	1200	1200
7	Laser/W	400	400	400
	Scanning speed/mm·s^{-1}	1000	1000	1000
8	Laser/W	400	400	400
	Scanning speed/mm·s^{-1}	1100	1100	1100
9	Laser/W	400	400	400
	Scanning speed/mm·s^{-1}	1200	1200	1200

strain changes. The strain and stress diagrams simulated by different process parameters are shown in Table 4 and Table 5.

According to the above analysis we can know that when the spot diameter and the powder thickness are fixed, the laser power is 200~400 W, and the scanning speed is 1000 and 1200 mm/s. When the laser power is 200W and the scanning speed is 1200 mm/s, the stress change value of the composite

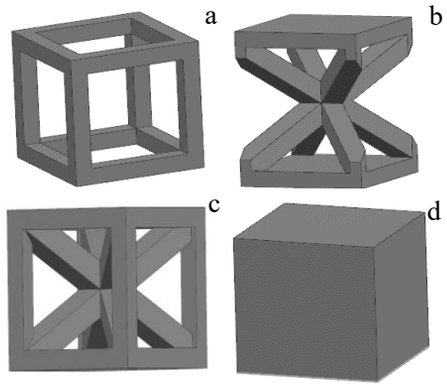

Fig.2 Monocellular body with four spatial pore structures: (a) regular hexahedral structure, (b) G7 structure, (c) composite structure, and (d) solid construction

structure is the smallest, and the strain change value is also the smallest.

Simufact Additive software was used to simulate the process parameters of printing and manufacturing. Therefore, we can get the best molding process parameters for printing and manufacturing, as shown in Table 6.

After the manufacturing was completed, the sample test piece was ultrasonically oscillated and cleaned by absolute ethanol and acetone in an ultrasonic cleaning machine for 30 min to remove excess titanium powder and oil stains. After the cleaning was completed, it was dried and packaged for use. The samples are shown in Fig.3.

Nova Nano SEM 430 scanning electron microscope (SEM) was used, the apparent morphology of three different spatial pore structures was observed as shown in Fig. 4. The solid structure does not require scanning electron microscope observation because there is no pore structure inside.

According to ISO13314: 2011 and using the ETM 205 D electronic universal testing machine (provided by Shenzhen WanCe Testing Equipment Co., Ltd), the room temperature compression test was carried out along the forming direction of the sample (*Z*-axis), and the size of the compressed sample was 10 mm×10 mm×20 mm. The compression loading rate was 1 mm/min, the test was carried out until the deformation

Table 4 Strain changes under different process parameters

Technological parameter		Experiment No.	Strain		
Laser power/W	Scanning speed/mm·s^{-1}		Regular hexahedral structure	G7 structure	Composite structure
200	1000	1	0.37217	0.34719	0.32021
	1100	2	0.35561	0.34384	0.44387
	1200	3	0.33623	0.33660	0.28965
300	1000	4	0.40901	0.40306	0.39789
	1100	5	0.39778	0.3796	0.37880
	1200	6	0.39164	0.35836	0.36157
400	1000	7	0.46296	0.47297	0.45697
	1100	8	0.44278	0.45086	0.43704
	1200	9	0.42690	0.42897	0.41900

Table 5 Stress changes under different process parameters

Technological parameter		Experiment No.	Stress/MPa		
Laser power/W	Scanning speed/mm·s^{-1}		Regular hexahedral structure	G7 structure	Composite structure
200	1000	1	1184.40	1185.84	1153.94
	1100	2	1178.32	1182.94	1147.46
	1200	3	1175.66	1180.64	1145.31
300	1000	4	1237.67	1203.93	1215.26
	1100	5	1220.70	1198.56	1208.35
	1200	6	1207.32	1194.36	1201.99
400	1000	7	1280.96	1227.59	1232.53
	1100	8	1267.44	1218.44	1227.85
	1200	9	1256.50	1211.15	1222.45

Table 6 Process parameters of Ti6Al4V formed by SLM

Laser power/W	Scanning speed/ mm·s^{-1}	Hatch spacing/ mm	Layer thickness/ mm	Atmosphere
200	1200	0.1	0.03	AR

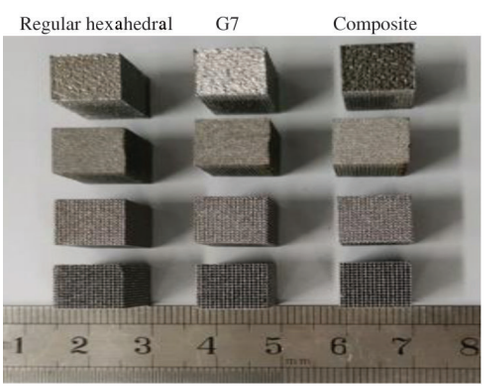

Fig.3 Physical object manufactured by SLM

of the test piece stops between 2 and 5 mm, and the experimental data was automatically recorded by the computer. The force-displacement curve can be simulated, and then the curve was converted into a compressive stress-strain curve. The compressive elastic modulus and compressive strength of the sample can be obtained from the compressive stress-strain curve. The sample specimens of each pore structure were measured more than three times and the average value was calculated.

Using the collected experimental data, the stress-strain curve diagram, compressive elastic modulus and compressive strength of the samples under static compression conditions can be obtained according to the following formula.

$$\sigma_P = \frac{F}{A_0} \tag{1}$$

$$\varepsilon_P = \frac{\Delta L}{L_0} \tag{2}$$

$$E_C = \frac{\sigma_P}{\varepsilon_P} \tag{3}$$

where F is the compressive load (kN) applied by the microcomputer-controlled electronic universal testing machine; A_0 is the initial cross-sectional area (cm^2) of the samples; L_0 is the initial effective length of the specimen (cm); σ_P is the stress of the specimen; ε_P is the strain of the specimen; E_C is the compression modulus of elasticity (MPa) of the test piece.

In order to conduct comparative experiments on three different spatial pore structures, we took solid-structure specimens and three different spatial pore structures together to conduct the compression experiment, and then carried out a comprehensive comparative study. The slope of a line is obtained by linearly fitting the linear elastic stage of static compression stress-strain curve, which is the corresponding

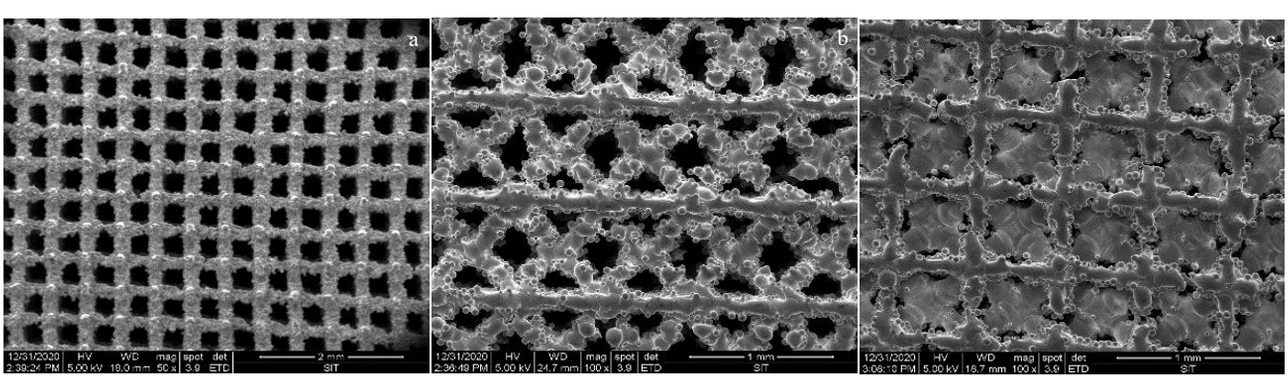

Fig.4 SEM morphologies of three different spatial pore structures: (a) regular hexahedral structure, (b) G7 structure, and (c) composite structure

compression elastic modulus. Fig. 5 shows the static compressive stress-strain curves of samples with different spatial pore structures. Each curve is drawn by taking the average of three or more experimental results.

As shown in Fig. 5, it can be seen from the static compressive stress-strain curve that during the quasi-static loading process, the stress-strain curves of the four different pore structures have basically the same change trend within the range of 0%~20% strain. But, the reduction ratio of the picture affects the actual size of the picture. The coordinate ratio of the four curves affects the comparison of the early stage. Experiments have a certain error, but the actual error is within the scope of the standard error.

The trend of linear correlation rises, and it belongs to the linear elastic stage. At this stage, the ratio of the ordinate to the abscissa satisfies Hooke's law, and the value of the ratio is the compressive elastic modulus of the samples.

According to the results of this experiment, the compressive stress-strain curves of different spatial pore structures can be divided into elastic stage, strengthening stage, and densification stage. The first stage is the elastic stage. At this stage, the stress and strain show a positive correlation growth, which is in the elastic deformation stage. After unloading the compressive force, the porous structure specimen can automatically return to its original state. The second stage is the strengthening stage. As the stress continues to be loaded, the stress gradually grows in a parabolic mode, and the stress growth is not as rapid as the linear elastic phase, which is determined by the porous structure itself. The porous structure at this time has not been completely compressed and deformed, which is gradually changed to a solid structure. At this stage, the specimens with different pore structures yield and fail from the weak point or the stress concentration area. The third stage is densification stage. As the strain continues to increase, the stress on the porous structure of the specimen continues to increase. In this stage, the porous structure unit slowly becomes a dense state, and then due to the increase in stress, the porous structure is compacted and crushed according to different pore structures.

When entering the densification stage, the stress on the sample reaches the highest point, and the porous structure is collapsed by compression deformation. The stress steadily increases with the strain, and gradually reaches a stress peak, and finally, the stress drops suddenly. This peak stress is the maximum compressive strength of the porous structure. The sample test piece is densely compacted or broken. The pore edges of the porous structure are also completely collapsed, and the opposite pore edges are in contact with each other, and the porous structure is compressed and collapsed.

At the same time, under the same pore size and different spatial pore structure, the linear elastic stage of the composite structure sample has a more suitable slope, that is, a suitable compressive elastic modulus, which meets the requirements of the implant, and the suitable elastic modulus can effectively enhance the bonding state of the implant bone interface.

The detailed information of the maximum compressive force, compressive elastic modulus, and compressive strength of different pore structures are shown in Table 7. Based on the compressive elastic modulus, it is possible to find the best state meeting the implant implantation standards and the implant-bone interface combination. Considering the stability of compression deformation, the toughness of compression deformation, and the comprehensive biomechanical properties, we believe that the specimen of the composite

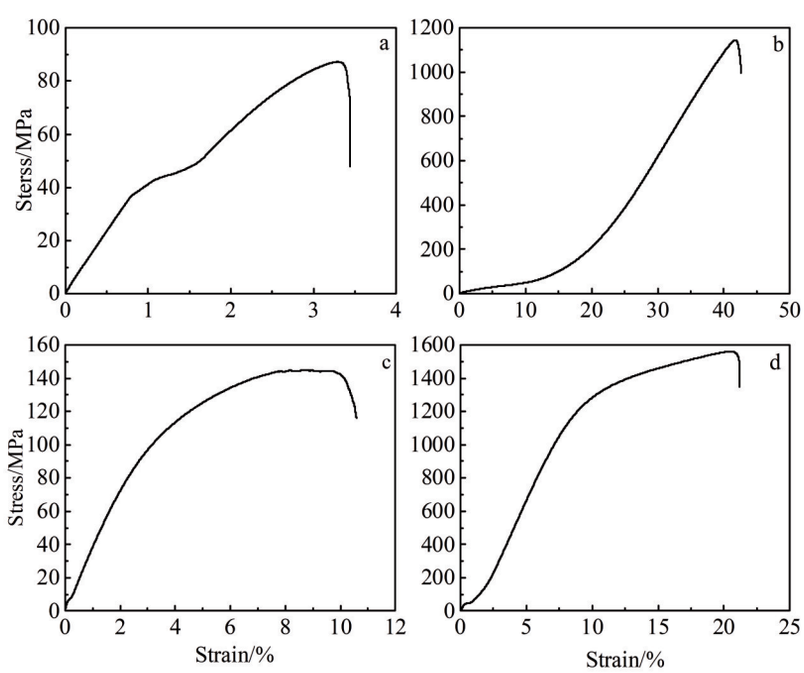

Fig.5 Stress-strain curves of different spatial pore structures: (a) regular hexahedral structure, (b) G7 structure, (c) composite structure, and (d) solid structure

Table 7 Mechanical properties of different space pore structures

Mechanical property	Regular hexahedral structure	G7 structure	Composite structure	Solid structure
Most condensation force/kN	8.722	114.421	14.487	156.198
Compressive elastic modulus/MPa	1460	1530	1300	5590
Compressive strength/MPa	111	1460	184	1990

structure is more suitable as the porous structure of the implant.

From the point of view of the maximum compression force, the maximum compression force will affect the service life of the specimen, and the compression force will affect the service life of the dental implant. For the composite structure, the value of the maximum compressive force is just in the middle level of these different spatial pore structures, which meets the implantation standards of dental implants. From the point of view of the compressive elastic modulus, the elastic modulus of the specimen must match the elastic modulus of the implant, that is, when the implant-bone interface is combined, the approximate elastic modulus must be reached, otherwise "stress shielding" will occur. In order to reduce the occurrence of this phenomenon, we choose a specimen with a smaller elastic modulus as the design of the porous structure of the dental implant. From the point of view of compressive strength, the compressive strength will affect the stress of the implant. For the composite structure, the compressive strength meets the standard of the implant-bone interface. In summary, selecting the porous structure specimen of the composites as the structural model of the dental implant can better promote the growth and bonding of the implant-bone interface.

3 Conclusions

1) Ti6Al4V alloy samples with different spatial hole structures formed by SLM can accurately process dental implants with different spatial hole structures. The best manufacturing process can be obtained through Simufact Additive software: the laser power is 200 W, the scanning speed is 1200 mm/s, the spot diameter is 0.1 mm, and the powder thickness is 0.03 mm.

2) The elastic modulus of titanium alloy with solid structure is 5590 MPa and its compressive strength is 1990 MPa. The elastic modulus of porous dental implant with composite structure is 1300 MPa and its compressive strength is 184 MPa. The porous structure has excellent comprehensive properties. The elastic modulus and compressive strength of implant with porous structure are better than those of implant with solid structure, which shows the advantage of porous structure in implant.

3) The pore structure can be adjusted to meet the biomechanical properties of different implants.

References

1 Branemark P I, Adell R, Breine U *et al. Scand J Plast Reconstr Surg*[J], 1969, 3(2) :81

2 Lin Ye. *Oral Implantology*[M]. Beijing: Peking University Medical Press, 2014 (in Chinese)

3 Lazzara R J. *Int J Periodontics Restorative Dent*[J], 1989, 9(5): 332

4 Liu P S, Chen G F. *Porous Solid Materials*[M]. Beijing: Tsinghua University Press, 2014

5 Ding Yubao, Yang Jianjun, Geng Xinjie *et al. Qilu Medical Journal*[J], 2010, 25(4): 331 (in Chinese)

6 Niu Jingzhe, Sun Zhonggang, Chang Hui *et al. Rare Metal Materials and Engineering* [J], 2019, 48(5): 1697 (in Chinese)

7 Wang H J, Yang F, Guo Z M *et al. Rare Metal Materials and Engineering*[J], 2021, 50(2): 709 (in Chinese)

8 Moin D A, Hassan B, Parsaa *et al. Clin Oral Implants Res*[J], 2014, 25(5): 598

9 Mangano F G, Cirotti B, Sammons R L *et al. Lasers Med Sci*[J], 2012, 27(6): 1241

10 Zhang Xiaowei, Liu Hongxi, Jiang Yehua *et al. Rare Metal Materials and Engineering*[J], 2012, 41(1): 178 (in Chinese)

11 Li Qing, Zhao Guorui, Ma Wenyou *et al. Material Review*[J], 2020, 34(4): 4073 (in Chinese)

12 Kanto Makoto, Fukunishi Shigeo, Fukui Tomokazu *et al. Arthroplasty Today*[J], 2020, 6(4): 894

13 Raffa Maria Letizia, Nguyen Vu Hieu, Hernigou Philippe *et al. Journal of Orthopaedic Research: Official Publication of the Orthopaedic Research Society*[J], 2021, 39(6): 1174

14 Barba D, Alabort E, Reed R C. *Acta Biomaterialia*[J], 2019, 97: 637

15 Giannitelli S M, Accoto D, Trombetta M *et al. Acta Biomaterialia*[J], 2014, 10(2): 580

16 Zhang B J, Li J, He L *et al. Acta Biomaterialia*[J], 2020, 115: 431

17 Dolder J V D, Farber E, Spauwen P H M *et al. Biomaterials*[J], 2003, 24(10): 1745

18 Xu Yangli, Zhang Dongyun, Hu Songtao *et al. Rare Metal Materials and Engineering*[J], 2020, 49(5): 1736 (in Chinese)

19 Liu P S, Ma X M. *Materials and Design*[J], 2020, 188: 108 413

20 Liu P S, Ma X M. *Multidiscipline Modeling in Materials and Structures*[J], 2021, 17(4): 814

21 Gonen Semih, Soyoz Serdar. *Structures*[J], 2021, 30(12): 378

22 Ghasemi A R, Razi E, Banisi S. *Advanced Powder Technology* [J], 2020, 31(4): 1365

23 Li S J, Li X K, Hou W T *et al. Science China-Materials*[J], 2018, 61(4): 525

24 Dhyah A, Ika K, Sugeng S *et al. Materials Research Express*[J], 2021, 8(1): 12 001

25 Liu Y J, Li S J, Zhang L C *et al. Scripta Materialia*[J], 2018, 153: 99

26 Sibiryakov B, Leite L W B, Sibiriakov E. *Journal of Applied Geophysics*[J], 2021, 186: 104 261
27 Zhang Wenyan, Xi Zhengping, Fang Ming *et al. Rare Metal Materials and Engineering*[J], 2008, 37(7): 1129 (in Chinese)
28 Qiao Jichao, Xi Zhengping, Tang Huiping *et al. Rare Metal Materials and Engineering* [J], 2009, 38(S3): 267 (in Chinese)
29 Yang Guang, Wang Bingyu, Zhao Shuo *et al. Rare Metal Materials and Engineering*[J], 2021, 50 (7): 2641 (in Chinese)
30 Gao Ruining, Xiong Yinze, Zhang Hang *et al. Rare Metal Materials and Engineering*[J], 201, 50(1): 249 (in Chinese)
31 Wang Yunda, Yang Yongqiang, Song Changhui *et al. Chinese Journal of Nonferrous Metals*[J], 2014, 24(10): 2497 (in Chinese)
32 Yuan Wanda. *Thesis for Master*[D]. Guangzhou: South China University of Technology, 2019 (in Chinese)

选区激光熔化制备多孔结构Ti6Al4V合金的力学性能

张建国[1]，黄道宇[1]，胡凤玲[2]，陈　晨[1]，宋　亮[3]，周　琼[1]，张而耕[1]
(1. 上海应用技术大学 机械工程学院 上海物理气相沉积(PVD)超硬涂层及装备工程技术研究中心，上海 201418)
(2. 复旦大学附属中山医院 口腔科，上海 200032)
(3. 复旦大学附属上海市第五人民医院 口腔科，上海 200240)

摘　要：采用Simufact Additive软件，通过正交实验的方法，对激光选区融化（SLM）制备多孔结构Ti6Al4V合金的最优化工艺路线进行了模拟。结果表明，激光功率200 W，扫描速度1200 mm/s，光斑直径0.1 mm，粉末厚度0.03 mm为最佳加工参数。根据优化参数通过SLM加工制造了不同孔隙结构的Ti6Al4V样件，通过扫描电镜观察发现，在该工艺下加工出的多孔结构具有较好的保真度。通过压缩实验，比较分析实心及不同孔隙结构的抗压强度及弹性模量，得出复合结构作为种植体的结构模型可以更好满足种植体的力学性能要求。

关键词：激光选区融化技术；Ti6Al4V合金；多孔结构；力学性能

作者简介：张建国，男，1979年生，博士，副教授，上海应用技术大学机械工程学院，上海物理气相沉积（PVD）超硬涂层及装备工程技术研究中心，上海 201418，E-mail：jgzhang98328@163.com